

The 2016 Feb 19 outburst of comet 67P/CG: an ESA Rosetta multi-instrument study

E. Grün,^{1,2★} J. Agarwal,³ N. Altobelli,⁴ K. Altwegg,⁵ M. S. Bentley,⁶ N. Biver,⁷ V. Della Corte,⁸ N. Edberg,⁹ P. D. Feldman,¹⁰ M. Galand,¹¹ B. Geiger,⁴ C. Götz,¹² B. Grieger,⁴ C. Güttler,³ P. Henri,¹³ M. Hofstadter,¹⁴ M. Horanyi,² E. Jehin,¹⁵ H. Krüger,³ S. Lee,¹⁴ T. Mannel,⁶ E. Morales,¹⁶ O. Mousis,¹⁷ M. Müller,¹⁸ C. Opitom,¹⁵ A. Rotundi,^{8,19} R. Schmied,^{6,20} F. Schmidt,²¹ H. Sierks,³ C. Snodgrass,²² R. H. Soja,²¹ M. Sommer,²¹ R. Srama,²¹ C.-Y. Tzou,⁵ J.-B. Vincent,³ P. Yanamandra-Fisher,²³ M. F. A’Hearn,²⁴ A. I. Erikson,⁹ C. Barbieri,²⁵ M. A. Barucci,⁷ J.-L. Bertaux,²⁶ I. Bertini,²⁷ J. Burch,²⁸ L. Colangeli,²⁹ G. Cremonese,³⁰ V. Da Deppo,³¹ B. Davidsson,³² S. Debei,³³ M. De Cecco,³⁴ J. Deller,³ L. M. Feaga,²⁴ M. Ferrari,⁸ S. Fornasier,⁷ M. Fulle,³⁴ A. Gicquel,³ M. Gillon,¹⁵ S. F. Green,²² O. Groussin,¹⁷ P. J. Gutiérrez,³⁵ M. Hofmann,³ S. F. Hviid,³⁶ W.-H. Ip,³⁷ S. Ivanovski,⁸ L. Jorda,¹⁷ H. U. Keller,¹² M. M. Knight,²⁴ J. Knollenberg,³⁶ D. Koschny,²⁹ J.-R. Kramm,³ E. Kührt,³⁶ M. Küppers,⁴ P. L. Lamy,³⁸ L. M. Lara,³⁵ M. Lazzarin,²⁵ J. J. López-Moreno,³⁹ J. Manfroid,¹⁵ E. Mazzotta Epifani,⁴⁰ F. Marzari,²⁵ G. Naletto,^{27,41} N. Oklay,³ P. Palumbo,^{8,19} J. Wm. Parker,⁴² H. Rickman,^{32,43} R. Rodrigo,^{4,44} J. Rodríguez,³⁹ E. Schindhelm,⁴² X. Shi,³ R. Sordini,⁸ A. J. Steffl,⁴² S. A. Stern,⁴² N. Thomas,⁵ C. Tubiana,³ H. A. Weaver,⁴⁵ P. Weissman,⁴⁶ V. V. Zakharov^{7,47} and M. G. G. T. Taylor²⁹

Affiliations are listed at the end of the paper

Accepted 2016 August 17. Received 2016 August 2; in original form 2016 June 17

ABSTRACT

On 2016 Feb 19, nine Rosetta instruments serendipitously observed an outburst of gas and dust from the nucleus of comet 67P/Churyumov-Gerasimenko. Among these instruments were cameras and spectrometers ranging from UV over visible to microwave wavelengths, *in situ* gas, dust and plasma instruments, and one dust collector. At 09:40 a dust cloud developed at the edge of an image in the shadowed region of the nucleus. Over the next two hours the instruments recorded a signature of the outburst that significantly exceeded the background. The enhancement ranged from 50 per cent of the neutral gas density at Rosetta to factors > 100 of the brightness of the coma near the nucleus. Dust related phenomena (dust counts or brightness due to illuminated dust) showed the strongest enhancements (factors > 10). However, even the electron density at Rosetta increased by a factor 3 and consequently the spacecraft potential changed from ~ -16 V to -20 V during the outburst. A clear sequence

* E-mail: eberhard.gruen@mpi-hd.mpg.de

of events was observed at the distance of Rosetta (34 km from the nucleus): within 15 min the Star Tracker camera detected fast particles ($\sim 25 \text{ m s}^{-1}$) while $100 \mu\text{m}$ radius particles were detected by the GIADA dust instrument $\sim 1 \text{ h}$ later at a speed of 6 m s^{-1} . The slowest were individual mm to cm sized grains observed by the OSIRIS cameras. Although the outburst originated just outside the FOV of the instruments, the source region and the magnitude of the outburst could be determined.

Key words: comets: individual: 67P/Churyumov-Gerasimenko.

1 INTRODUCTION

In 2014 August the Rosetta spacecraft arrived at comet 67P/Churyumov-Gerasimenko (67P). Since then, the spacecraft has been accompanying the comet on its journey around the Sun (Glassmeier et al. 2007a). During that time Rosetta used all its instruments to closely study the nucleus and its activity. In 2015 August Rosetta and 67P passed through perihelion at a distance of 1.25 au from the sun, and a firework display of cometary outbursts was observed (Vincent et al. 2016b). Six months later on 2016 Feb 19 nine Rosetta instruments serendipitously observed an outburst of gas and dust from the nucleus of 67P. This paper is the first report of this most extensively studied cometary outburst.

The observations were carried out during the Rosetta mission extended phase, very close to the end of the intensive summer that the Southern hemisphere of the comet experienced between 2015 May and 2016 March. A large number of observations were under way in order to obtain final measurements to characterize the Southern hemisphere before it re-entered polar night, and to observe the return of the Northern hemisphere from its shorter polar night. Ground-based observations were most favourable during early 2016 because the comet was still relatively active (as exemplified by the event discussed in this paper) and was visible in the night sky as observed from Earth. During 2015 the spacecraft had been flying at greater distances from the comet than originally foreseen, in order to avoid the navigational interference caused by the appearance of dust particles in the star tracker cameras. Therefore, at perihelion the spacecraft was at a distance of around 400 km from the comet, as a result of the high dust fluxes produced at this time. The period discussed in this paper was particularly focused on achieving the lowest possible altitudes by orbiting in the terminator plane. As such, it was the first time the spacecraft had been within 50 km of the comet since 2015 April. These lower altitudes were designed to examine surface changes due to perihelion passage and the seasonal effects of the approach of equinox. In addition, an overall target for the mission had been to investigate active areas and jets from their origin at the surface of the comet to *in situ* at the spacecraft. However, such observations had been difficult to target specifically. Such a serendipitous event with the instrument coverage of 2016 February 19 was therefore most welcome. Earlier plans to perform an Activity Campaign by flying through a dust jet with all instruments monitoring the gas and dust environment and the source region on the nucleus underneath had been abandoned because of the star tracker interferences.

By 2016 February 19 the heliocentric distance had increased to almost twice the perihelion distance to 2.4 au. Rosetta flew hyperbolic arcs between 42 and 32 km with a speed relative to the comet centre of 0.174 m s^{-1} (Fig. 1). At 10:00 on Feb 19 the distance of Rosetta from the centre of the comet was 34.5 km, the angular size of the nucleus was about 8° , and the solar phase angle was 63° . Rosetta was above the Southern hemisphere of 67P on the morning side at local time 07:51:37 (referring to the illumination by the sun).

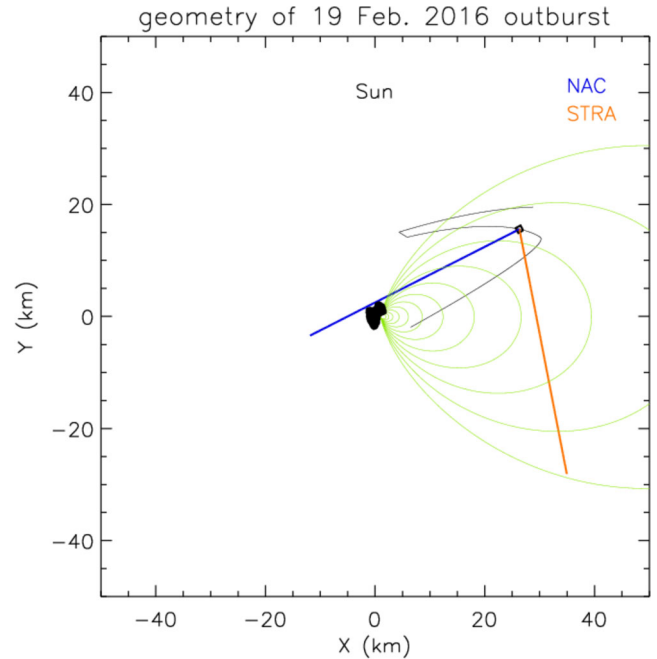


Figure 1. Observation geometry (right) in Sun-67P-Rosetta plane on Feb 19 10:00. Black line: projection of trajectory from 2016 Feb 15 to 24; square; Rosetta position; blue line: line of sight (LOS) of remote sensing instruments (OSIRIS NAC and WAC, Alice, NAVCAM); red line: projection of LOS of Star Tracker A (STR-A); green: schematic evolution of a dust plume.

The sub-S/C latitude was -30° and the longitude was 301° in the Cheops Reference Frame.

Science operations on Feb 19 called for (1) dust monitoring by the OSIRIS imaging system followed by (2) a global coma scan by the microwave instrument MIRO with the Alice UV spectrograph and OSIRIS co-riding. OSIRIS dust monitoring required off-limb pointing for the Narrow Angle Camera NAC and the Wide-Angle Camera WAC (Fig. 1), covering in duration at least a full nucleus rotation of about 12 h. The fourth remote-sensing instrument VIRTIS, an infrared imaging spectrometer, was monitoring the illuminated nucleus whenever allowed by the dust-monitoring pointings of OSIRIS and MIRO. All *in situ* instruments monitored, in parallel dust (GIADA), gas (ROSINA), and plasma (RPC). In addition the dust collectors of MIDAS were exposed to the environment all day. Science observation periods of about 4 h were interrupted by Nadir pointing navigation and maintenance activities of about 1 h and 0.5 h duration, respectively. The latter technical activities involved observations by the Star Tracker (STR) and the Navigation Camera (NAVCAM). The OSIRIS dust monitoring campaign, which was staring just above the sub-solar limb ($\sim 4^\circ$ from Nadir, Fig. 2), started February 18 UT 21:52:51 and ended on the next day at 12:42:09. The following global coma scan by MIRO required pointing of up to 70° away from Nadir.

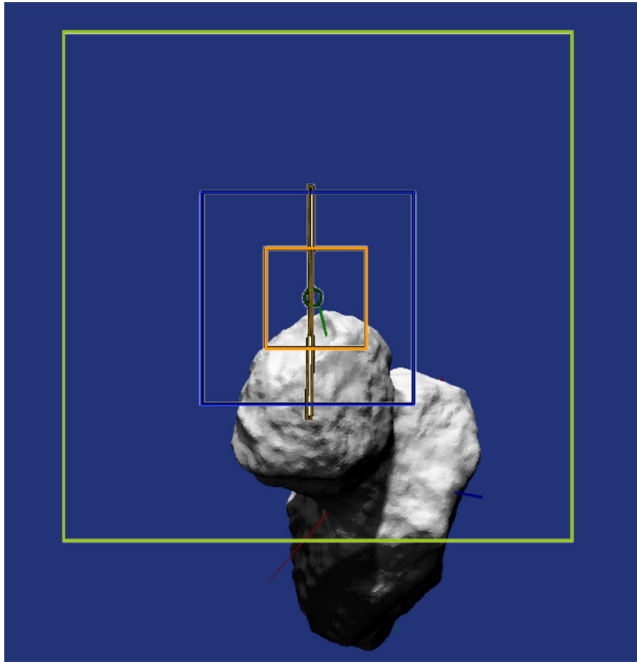


Figure 2. Model image (generated by the CG Model viewer <https://planetgate.mps.mpg.de:8114/>) showing the nucleus and its illumination at 09:40 in the perspective from Rosetta. The Sun is up. The squares of decreasing size are the fields of view (FOVs) of the WAC, NAVCAM, and NAC cameras, respectively. The vertical bar represents the Alice slit and the small circle is the MIRO sub-millimetre beam. The short red, dark green, and blue bars indicate the principle axes of the nucleus.

About 2 d after the data were taken they were transmitted to the ground and accessible by the instrument teams. In the morning of February 22 the GIADA team reported a large flux of compact dust particles between 10:00 and 13:00 on February 19. The operations team responded that the STR saw a huge increase in background noise in the same time period. The ROSINA team reported a correlated peak in the neutral gas density. Observers on the ground suggested from preliminary photometry of 67P with the Transiting Planets and Planetesimals Small Telescope (TRAPPIST) at ESO’s La Silla Observatory an increase in total brightness. A search of the NAVCAM images resulted in images that showed local dust coma brightness enhancements near the nucleus. In addition the Langmuir probes of the Rosetta Plasma Consortium (RPC-LAP) found the spacecraft potential dropped from about -15 to -20 V by about 10:00 on Feb 19 and then recovered within a few hours. In the following days MIRO also reported changes in the coma temperature in the same time period. MIDAS also collected plenty of dust during the collection period that included February 19. The break-through in understanding of what had happened came about three weeks later when the OSIRIS team presented WAC and NAC images that showed the history of the outburst on February 19 and indicated the potential source region.

In Section 2 we give a detailed description of the observations by various instruments, including some ground-based observations. In Section 3 the timing of the different observations is compared in order to pin-down the exact time of the outburst and identify the potential source region and the magnitude of the outburst. A summary of the results and a comparison with previous outbursts during the perihelion passage is given in Section 4 including a discussion of further studies and potential mechanisms.

2 OBSERVATIONS

Details of the positive observations of the outburst from Rosetta and ground-based astronomical observations are discussed in the following sections. Their order reflects the approximate time order of the maximum signals recorded. First were the OSIRIS and NAVCAM series of camera images and the ALICE UV observations, followed by the MIRO microwave observations, the RPC plasma and the ROSINA COPS gas density measurements. Later came the Star Tracker brightness measurements, and the GIADA dust detections and the MIDAS dust collections. These Rosetta observations are complemented by ground-based observations of the coma and tail.

No relevant observations were made by VIRTIS because the VIRTIS-Mapper was looking at the sub-solar limb, with the slit located away from the source region. No dust was collected by the COSIMA dust mass analyser during February 19 because it was in the dust analysing mode during that period. The Radio Science Investigation (RSI) did not see a sign of the outburst in the radio signal from Rosetta. Additionally, measurements of the gas drag from momentum wheel measurements by the attitude and articulation system of the spacecraft were unfavourable during the time period of the outburst.

2.1 OSIRIS

The Optical, Spectroscopic, and Infrared Remote Imaging System (OSIRIS, Keller et al. 2007) on board the Rosetta spacecraft consists of a Narrow- and a Wide Angle Camera (NAC) and (WAC), each having a 2048×2048 pixel CCD detector, and fields of view (FOVs) of approximately $2^\circ \times 2^\circ$ and $12^\circ \times 12^\circ$, respectively. The cameras have regularly imaged the nucleus and the coma of 67P since 2014 March in 25 broad- and narrow-band filters covering the wavelength range 240–1000 nm (Sierks et al. 2015). The standard data processing on ground comprises bias-subtraction, flat-fielding, correction for distortion of the optical path, and flux calibration relative to standard stars.

From Feb 18 21:56 to Feb 19 12:10, OSIRIS obtained one NAC and two WAC images approximately every 30 min. The NAC images were taken in the orange filter (centred at 649 nm with a bandwidth of 85 nm, exposure time 3.75 s), and the WAC images were obtained using the green (537 nm, 63 nm, 3 s) and red (630 nm, 157 nm, 1.5 s) filters. At the 34.5 km distance of the comet from the spacecraft, the FOVs covered 1.4 km (NAC) and 6.9 km (WAC). The instrument boresights were pointed at the sub-solar limb. The WAC images cover a significant part of the nucleus.

As shown by Fig. 3, up until Feb 19 9:10 the images show a typical coma composed of faint dust structures. The nucleus has deep shadows and illuminated surfaces that are saturated on the detector, because the exposure times were optimized to capture the faint dust coma. The WAC images obtained at 09:40, however, show a brightening strong enough to saturate the detector in a region where the nucleus should be in shadow. By 10:10, the bright cloud had expanded across the entire WAC FOV, saturating the detector in front of the whole visible part of the big nucleus lobe. At 10:40 the overall coma brightness had diffused, but a large part of the shadowed nucleus was still hidden behind bright foreground dust. The dust diffused slowly in the following images, and several narrow coma structures became visible. These could be related to the outburst, but some may also reflect the typical activity of this region and local time.

The coma surface brightness as a function of time was measured in two reference areas in the FOVs of NAC (above the sun-lit limb)

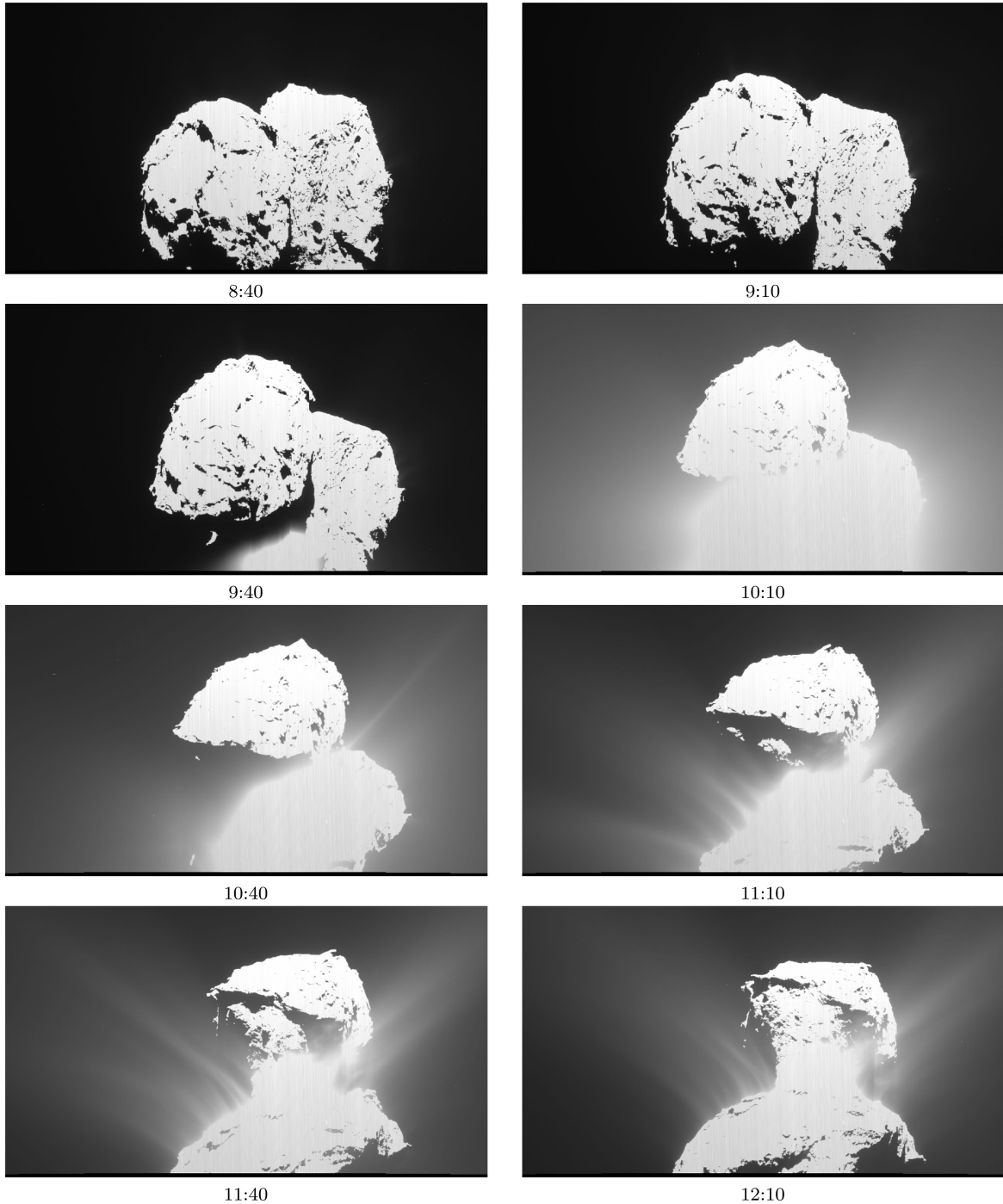


Figure 3. OSIRIS WAC images taken at 08:40, 09:10, 09:40, 10:10, 10:40, 11:10, 11:40, and 12:10, respectively. Each image is about $11^{\circ}5 \times 6^{\circ}2$ in size, they were obtained in the broad-band green filter with 3 s exposure time. The image brightness is scaled according to the square root of the measured flux, with minimum and maximum values of 1.5×10^{-7} (black) and $1.5 \times 10^{-4} \text{ W m}^{-2} \text{ sr}^{-1} \text{ nm}^{-1}$ (white). The Sun is at the top.

and WAC (in the lower left corner of the image). These were chosen to be sufficiently distant from the saturated area and from the limb, in order to minimize rotation-induced changes of the brightness as a consequence of changing limb-distance from the irregularly shaped nucleus. In the WAC reference area, located near the source region, the surface brightness of the coma (corresponding to the total dust cross-section) increased by two orders of magnitude between 09:40 and 10:10, and decreased back to a factor 10 above the pre-outburst level in the last image obtained at 12:10 (Fig. 4).

The NAC images were zoomed and stretched to such detail that individual grains became visible. After subtracting the local background the image sequence shows a transition from a point-like granularity (grains that were distant or slow enough to appear as points) to a more linear texture dominated by grains either close or fast enough to be trailed across several pixels. The transition occurred between 11:10 and 11:40.

In the afternoon of February 19, from 14:30 to 21:30, OSIRIS took NAC and WAC images during a MIRO Great Circle Scan

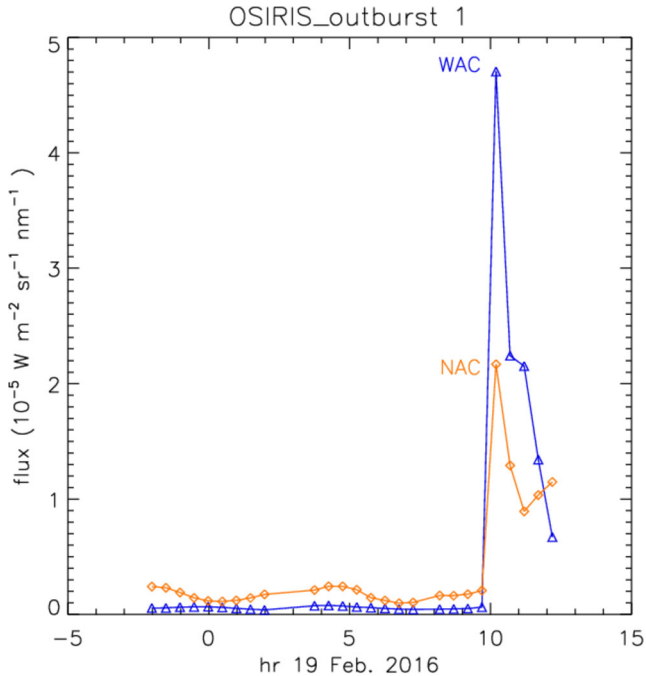


Figure 4. Surface brightnesses measured in the WAC and NAC reference areas.

pointing most of the time far from nadir. At 14:30, the coma surface brightness was still one order of magnitude higher than at reference epochs with similar pointing. It decreased to normal level at 21:30, i.e. about one spin period after the start of the outburst.

2.2 NAVCAM

The Navigation Camera (NAVCAM) is part of the spacecraft subsystems. It is used by the Flight Dynamics team in order to determine

the relative position between Rosetta and the comet nucleus. Its images are therefore essential for safely navigating the spacecraft in the comet environment. In addition, context images for scientific observations are also scheduled on request of the instrument teams.

There are two identical NAVCAMs on board the spacecraft, although only one of them is used in nominal operations. The camera's field of view is $5^\circ \times 5^\circ$ and its CCD detector consists of 1024×1024 pixels. The spectral sensitivity covers the visible wavelength range from approximately 550 to 850 nm. A mechanism makes it possible to select between different optical elements with or without attenuation coating. There are no spectral filters.

During the period of the outburst event NAVCAM context images without attenuation were acquired at 08:21, 10:14, and 12:29. Afterwards a navigation raster comprising four images at 12:51, 12:55, 13:01, and 13:05 was carried out with the attenuation filter. The uncalibrated data are available in the ESA Planetary Science Archive (Geiger & Barthelemy 2016).

A preliminary version of the foreseen radiometric calibration procedure (Geiger et al., in preparation) was applied in order to transform the raw pixel values to average spectral radiance values in the broad visible wavelength range. Fig. 5 depicts the two images acquired at 12:29 and 12:55. The NAVCAM images show that the collimated dust emission seen in the last images of the OSIRIS sequence (cf. Fig. 3) continues as the nucleus rotates. In addition to the diffuse component a few individual objects can be seen in the coma. However, from the images it is not possible to determine the distance from the spacecraft and hence the size of these objects.

2.3 Alice

Alice is a far-ultraviolet (70–205 nm) imaging spectrograph on board Rosetta that, amongst multiple objectives, is designed to observe emissions from various atomic and molecular species from within the coma of comet 67P (Feldman et al. 2015) as well as reflected solar radiation from both the nucleus and the dust coma

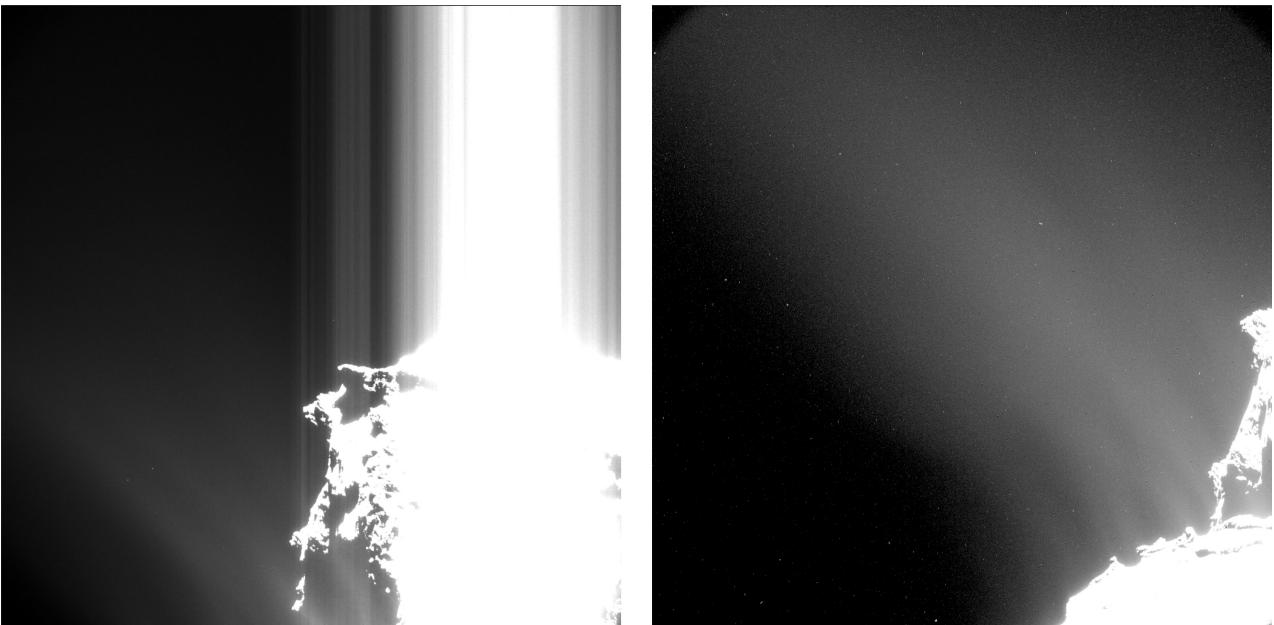


Figure 5. NAVCAM images acquired at 12:29 (left) and 12:55 (right). The first image was taken without attenuation filter and 0.01 s exposure time. The vertical structures towards the top right are blooming artefacts due to saturation on parts of the nucleus. The second image is part of a navigation raster with attenuation filter and 1.75 s exposure time. The grey-scales were adapted such that the maximum (white colour) corresponds to $1 \times 10^{-4} \text{ W m}^{-2} \text{ sr}^{-1} \text{ nm}^{-1}$.

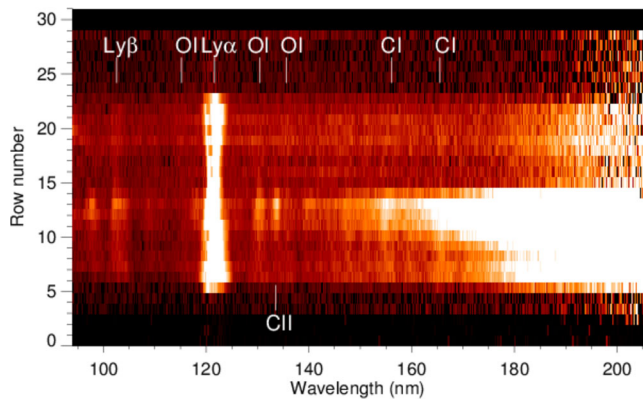


Figure 6. An Alice spectral image beginning at UTC 11:19:44 showing the solar reflected radiation from the nucleus in the lower right. Dust in the coma shows up in the upper right. The orientation of the slit is as shown in Fig. 2. The integration time was 1814 s.

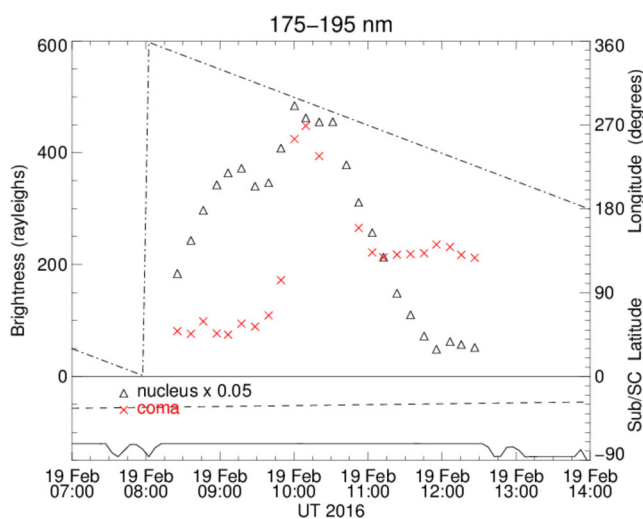


Figure 7. Light curve of the reflected solar radiation (175–195 nm) seen by Alice. The times represent the mid-points of each 10-min integration. The enhancement in emission seen towards the nucleus is superimposed on a smooth variation due to changes in geometry as the comet rotates. The sub-spacecraft longitude (dot-dashed line) and latitude (dashed line) are also shown. The line near the bottom shows the $3^{\circ}58'$ offset of the boresight from nadir towards the Sun.

(Feaga et al. 2015; Stern et al. 2015). The spectrograph slit is in the shape of a dog bone, $5^{\circ}5'$ long, with a width of $0^{\circ}05'$ in the central $2^{\circ}0'$, while the ends are $0^{\circ}10'$ wide, giving a spectral resolution between 0.8 and 1.2 nm for extended sources that fill its field of view. Each spatial pixel or row along the slit is $0^{\circ}30'$ long. Details of the instrument have been given by Stern et al. (2007).

In particular, Alice is able to address the timing and duration of the event. The Alice observations were made with the small lobe of the nucleus in the lower half of the slit and the coma above the sunward limb in the upper half, as shown in Fig. 2. A spectrum taken on Feb 19 11:19:44 is shown in Fig. 6. A light curve derived from the Alice spectra is shown in Fig. 7. In two successive 10-min histograms beginning at UT 09:45:59 Alice observed a ~ 50 per cent increase in brightness in the direction of the small lobe of the nucleus. Considering the 10-min integration time of the Alice data, the onset time is consistent with that reported by the other remote sensing instruments on Rosetta. At the same time the dust coma

brightness increased by a factor ~ 5 and remained at that level for ~ 30 min. The following histograms had contamination of the coma from a bright star in the field of view leading to a 20-min data gap. From 11:10 until the end of the observation sequence at $\sim 12:30$ the coma brightness remained at a value of ~ 2.5 times the prior quiescent level. There were no further Alice observations with the same viewing geometry on February 19. The same data do not show any significant gas emissions at the time of the outburst.

2.4 MIRO

MIRO (Microwave Instrument for the Rosetta Orbiter) is a small radio telescope working at millimetre and submillimetre wavelengths (Gulkis et al. 2007). It has broad-band continuum receivers designed to measure the sub-surface properties of the nucleus and to study dust in the coma. MIRO also has a high-resolution spectrometer, which can be used to probe the abundance, temperature, and velocity of several coma gases, including H_2O . MIRO is calibrated against two internal targets approximately every 30 min, and can also be calibrated against dark sky measurements when looking far from the nucleus. Here we focus on some of MIRO's spectral observations during the outburst. A more complete description of MIRO's view of the outburst is in Hofstader et al. (in preparation).

MIRO is a single-pixel instrument. From about 08:10 to 12:30 on 2016 February 19 Rosetta was performing a stare above the sub-solar limb (Fig. 2). Most of that time MIRO's footprint was above the limb, but from about 09:30 to 11:00 the rotation of the nucleus brought parts of the surface into its line of sight.

Water vapour all along MIRO's line of sight contributes to the received signal, so interpreting the spectrum at all frequencies requires detailed consideration of the three-dimensional structure of the coma. Given the strength of the water line, however, there are frequencies at which the coma is optically thick, and MIRO senses only the gas relatively close to the spacecraft. The received signal is remarkably constant at these frequencies. Even as the nucleus moves into and out of MIRO's LOS, the signal does not change because the nearby gas screens the view of everything beyond it. Under these optically thick conditions, the amount of radio energy received is set by the rotational temperature of the gas.

Fig. 8 shows the radio emission from the coma at an optically thick frequency, expressed as a brightness temperature. The frequency chosen corresponds to the H_2^{16}O line centre for gas moving at 620 m s^{-1} towards the spacecraft. The H_2^{16}O spectrum in this region shows features indicative of being optically thick (Hofstader et al., in preparation) and the H_2^{18}O line shape confirms the gas expansion velocity is near 600 m s^{-1} . In the figure, the brightness temperature rise of the gas by about 30 K was starting just before 10:00 on February 19, followed by a slow decrease for several hours. At about 12:30 the spacecraft began pointing to different areas of the coma, and the measurements can no longer be directly compared to those shown. It is interesting to note that one nucleus rotation (about 12.4 h) before the outburst, the nucleus orientation and MIRO's observing geometry were similar to that during the outburst. Fig. 8 also shows that the temperature of the coma at that time (times from $-02:00$ to $00:00$) is consistent with the values measured just before the outburst. This demonstrates that the change occurring near 10:00 is not due to normal diurnal variations.

Hofstader et al. (in preparation) explore three possible explanations for the increase in coma temperature. One is that the gas during the outburst is coming from a source region on the nucleus with a significantly higher physical temperature than the normally sublimating regions. Another possibility is that the local gas

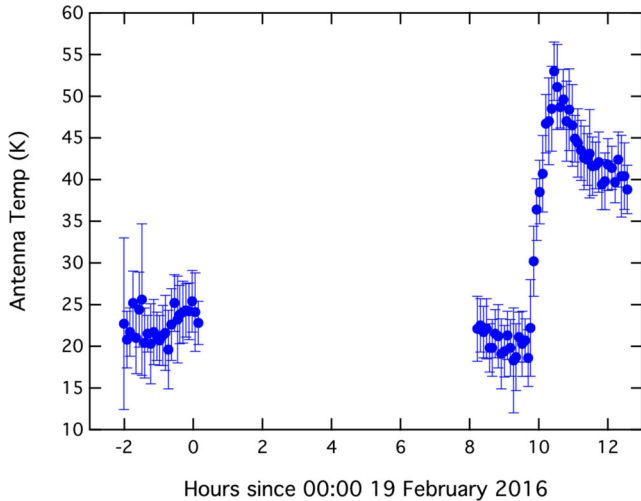


Figure 8. Time evolution of the H_2O excitational temperature of the gas near the spacecraft, as measured by gas moving at a velocity of 620 m s^{-1} towards the observer (see text). MIRO collected spectral data every 30 s. The indicated points represent a 5-min average of those data, with error bars being the rms deviation of the 10 spectra in each average.

density during the outburst, either above or below the surface, increased enough to alter the adiabatic cooling expected as the gas expands into a near vacuum. The third explanation we are exploring is that the gas is warmed by the dust either via collisions or radiation. Gas by itself cools adiabatically very quickly as it expands into space, whereas dust by itself can stay warm because it cools radiatively much more slowly.

An important clue, discussed later (see Fig. 18), is that the increase in gas temperature near the spacecraft observed by MIRO occurs several minutes after dust is first seen rising from the nucleus, but several minutes before the local gas density increases. Note that dust travelling at metres per second takes over an hour to travel from the nucleus to the spacecraft, while gas moving at 620 m s^{-1} takes only about a minute. The relative timing of rising dust at the surface, the increase in gas temperature at the spacecraft, and then the increase in gas density at the spacecraft, is not yet understood.

2.5 RPC

The Rosetta Plasma Consortium (RPC, Carr et al. 2007) is a suit of five plasma sensors to monitor the electro-magnetic field and the ionized environment around 67P. Among the RPC sensors, RPC-MIP (Mutual Impedance Probe, Trotignon et al. 2007) and RPC-LAP (Langmuir Probes, Eriksson et al. 2007) measure the plasma density. Following the increase in neutral density by a factor ~ 1.8 (ROSINA-COPS, Section 2.6), MIP and LAP observed a local plasma density increase by a factor $\sim 2.7\text{--}3$ during the outburst, both through the electron plasma frequency increase (MIP) and (negative) spacecraft potential increase (LAP), as shown in Figs 9 and 10. The spacecraft potential is proportional to the logarithm of the electron density. Note that a local decrease in the plasma density is observed just before the onset of the outburst, around 09:45. The energetic electrons observed during the outburst are colder than before and after the outburst, as suggested by RPC-IES electron spectra (Ion and Electron Spectrometer, Burch et al. 2007). This would be consistent with electron cooling during the outburst, in the region between the comet and the spacecraft. Such cooling may be the signature of an increase in electron-neutral col-

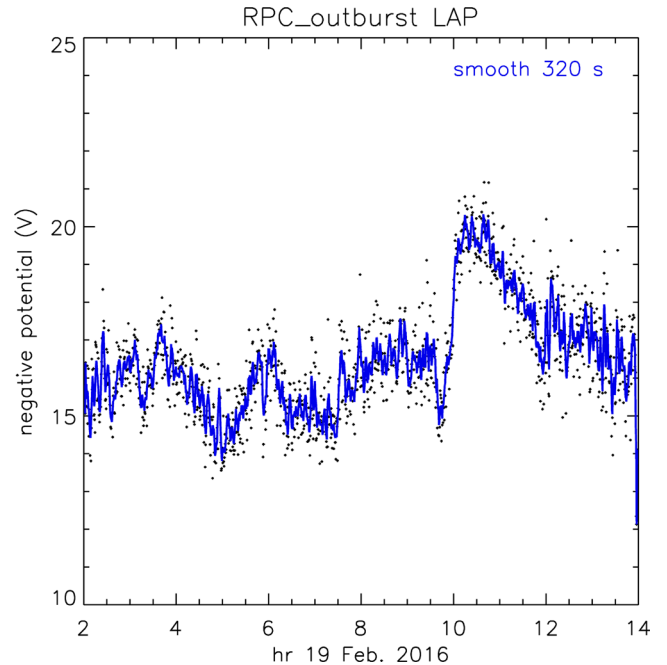


Figure 9. The negative spacecraft potential as determined by RPC-LAP. Individual measurements (dots) and smoothed signal (blue line).

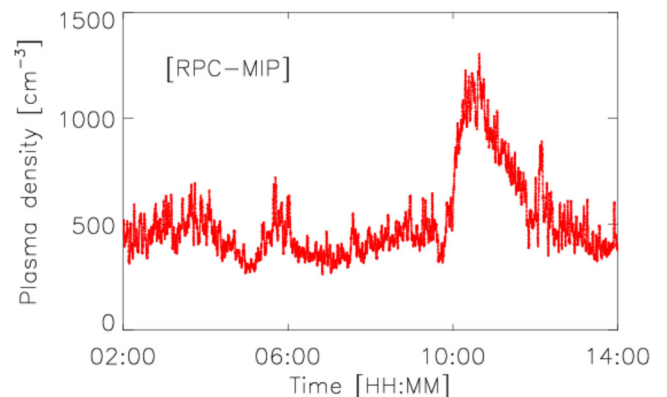


Figure 10. Plasma density measured by RPC-MIP.

lisions, which is consistent with the observed increase in the neutral density (Section 2.7). Those collisions may have increased the local ionization by electron impact in the region between the comet and the spacecraft. An increase in the ionization source closer to the comet could explain the significant relative increase in plasma density, which is larger than the relative increase in neutral density, observed at Rosetta during the outburst. However, other possible explanations exist, such as a reduced neutral outflow velocity or changes in composition. Further studies are needed to identify the exact mechanisms causing the variable plasma density as well as the faster plasma density decay compared to the neutral density decay. Finally, the plasma density relaxes to the pre-outburst value around 12:00 UT, faster than the neutral density, while cold electrons are still observed until 14:00 UT.

While the electron density increased, the average magnetic field measured by RPC-MAG (Magnetometer, Glassmeier et al. 2007b) increased slightly from 16 nT to 19 nT. This change was mostly in the y -direction, meaning the direction in the ecliptic that is perpendicular to the Sun–comet line. At the same time the power

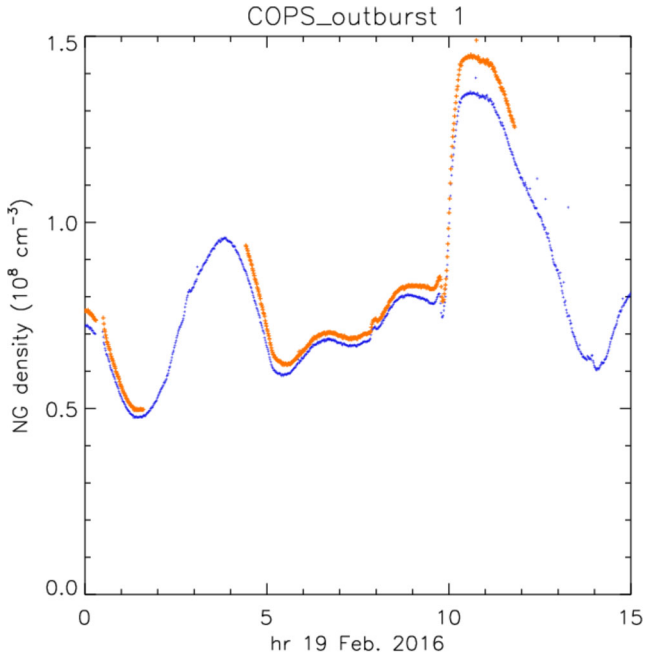


Figure 11. Neutral gas density (red) and uncalibrated COPS signal (blue, arbitrary units) during 2016 Feb 19. Calibration was only applied when DFMS measurements were available. During MR global coma scan starting at 13:00 the coma gas was contaminated by spacecraft outgassing.

spectral density in the range of 50–100 mHz decreased by about a factor 1/2.

2.6 ROSINA

ROSINA is designed for *in situ* measurements of the cometary coma gas density and composition (Balsiger et al. 2007). The instrument package consists of two complementary mass spectrometers (DFMS and RTOF) for neutrals and primary ions and a pressure sensor (COPS). ROSINA-COPS is an *in situ* instrument consisting of two separate sensors, described by Balsiger et al. (2007). The nude gauge (NG) measures the total ambient neutral gas number density at the spacecraft position and the ram gauge, which is normally pointing at the comet, measures the ram pressure of the outflowing gas of coma. All data presented in this study are from the NG sensor only. The neutral gas density is determined from the sensor signal as a linear combination of the abundances of the dominant species H_2O , CO_2 , CO , and O_2 which are obtained by DFMS spectrometer measurements (Hässig et al. 2015).

The neutral gas density is modulated by the spacecraft location around the nucleus and the nucleus illumination conditions. Because of the highly irregular shape of the nucleus, the gas production varies by about a factor of 2 depending on the face that is illuminated by the Sun (Bieler et al. 2015). On Feb 19 the neutral gas density (Fig. 11) showed fluctuations of up to 10^8 cm^{-3} due to the nucleus rotation. However, at $\sim 10:00$ the gas density rapidly increased to almost $1.5 \times 10^8 \text{ cm}^{-3}$ which is more than 50 per cent higher than the normal fluctuations at a similar nucleus phase.

2.7 Star Tracker

The autonomous attitude control system of the spacecraft relies on Star Tracker measurements as the main source of information (Buemi, Landi & Procopio 2000). The field of view of the Star

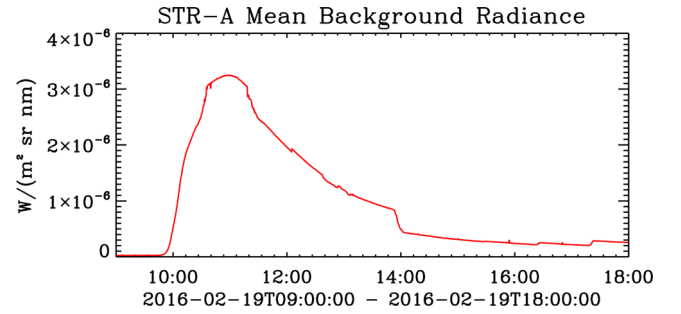


Figure 12. Temporal evolution of the mean background radiance measured by Star Tracker A (STR-A) during the outburst event. The results are derived from a housekeeping telemetry parameter which reports the mean background signal in 20×20 pixel windows around the (up to nine) tracked stars.

Tracker camera has a size of 16.4×16.4 . The characteristics of its CCD detector are identical to those of the NAVCAM, i.e. 1024×1024 pixels and a broad spectral sensitivity in the visible wavelength range.

For redundancy two identical Star Trackers are available (STR-A and STR-B). Although they are both mounted on the -X-face of the spacecraft, their boresight directions differ by $\sim 30^\circ$. In the period of interest STR-A was continuously active in the closed attitude control loop. In addition, STR-B was switched on for 15 min at around 13:00 UTC for a regular attitude acquisition test.

In their operational modes the Star Trackers track the positions and magnitudes of up to 9 stars in the field of view. Housekeeping telemetry downlinked to ground includes a parameter that reports the mean background signal in 20×20 pixel windows centred on the tracked stars. The value of this parameter quantifies the diffuse light contribution due to scattering by unresolved dust particles and provides valuable information about the temporal evolution of the outburst event.

We converted this parameter value into spectral radiance units by subtracting a bias value estimated from the available time series during the whole mission and by applying a calibration coefficient determined from the magnitude conversion relations specified by the manufacturer in the on-board software. The uncertainty of this rough radiance calibration is expected to be in the order of 50 per cent or better. The spectral radiance values should be understood as a weighted average over the broad visible sensitivity range.

The temporal evolution of the STR-A mean background radiance on February 19 is shown in Fig. 12. At the beginning of the depicted period the signal is at the noise level. However, shortly before 10:00 UTC the measured background radiance sharply increases, reaches its maximum at 11:00 UTC, and then slowly decreases. The step at about 14:00 UTC is due to a significant attitude change of the spacecraft due to the MIRO global coma scan. Before that time the spacecraft +Z-axis pointed towards the nucleus and consequently the STR-A boresight pointed 90° off-nucleus.

The radiance values measured by STR-B during its short operating period are in the same order as the STR-A results. Their quantitative difference is consistent with the different boresight directions of the two Star Trackers.

2.8 GIADA

GIADA (Grain Impact Analyzer and Dust Accumulator; Colangeli et al. 2007) consists of three sub-systems: (1) the Grain Detection System (GDS), which detects dust particles as they pass through a

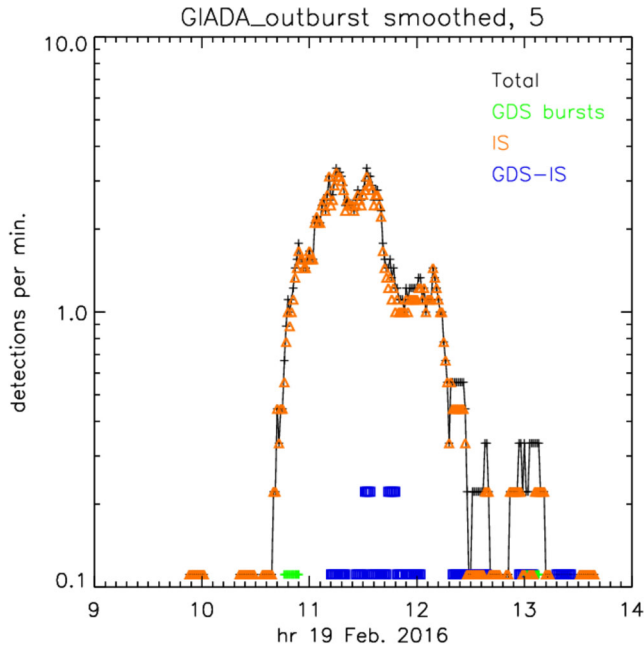


Figure 13. Rate of GIADA dust detections (total: black) and by its sub-systems GDS-IS (blue), IS (red), and GDS bursts (green). The individual counts were smoothed with a 9-min running average.

laser curtain and provides particle speeds and their optical cross-section; (2) the Impact Sensor (IS) measures particle’s momentum from their impact on a plate connected to five piezoelectric sensors, which combined with the GDS detection time provides the particle speed and mass; (3) the Micro Balances System (MBS) provides the cumulative dust flux of grains smaller than $10\ \mu\text{m}$ (Della Corte et al. 2014), by using five quartz crystal microbalances in roughly orthogonal directions. Calibration activity performed on GIADA by means of cometary analogues (Ferrari et al. 2014) mean that it is possible to convert the GDS signal to the dust particle geometrical cross-section (Della Corte et al. 2016a), and thus to constrain the particle density (Rotundi et al. 2015). GIADA disentangled two particle families (Della Corte et al. 2015) present in the 67P coma: high density aggregates (detected by GDS and IS together and by IS alone), i.e. compact particles, and low density porous aggregates (detected by GDS alone), i.e. fluffy particles. GIADA observed an exceptional dust detection rate on the 2016 February 19: 188 compact particles detected from 10:25:41 to 13:35:47 (Fig. 13) and 5 dust showers (Fulle et al. 2015) representing a total of 386 fluffy particles, 359 of which were detected from 17:27:35 to 17:28:00. The five dust showers are counted in the following only as five individual events since Fulle et al. (2015) suggest that the showers are caused by electro-static break-up of very fluffy agglomerates of sub-micron grains close to the Rosetta spacecraft. This is compared to a mean detection rate of ~ 3 compact particles/day for most of the month of February 2016. For the GDS-IS detections GIADA provides directly particle speed, mass, and density. However, some assumptions have to be made in order to acquire the same information from detections on IS alone (Della Corte et al. 2016b).

2.9 MIDAS

Micro-Imaging Dust Analysis System (MIDAS) is an atomic force microscope (AFM) coupled with a dust collection and handling system (Riedler et al. 2007; Bentley et al. 2016). Capable of resolutions down to the nanometre level, the AFM operates by scan-

ning a sharp tip over the sample and produces three-dimensional images of collected dust particles. During the outburst event MIDAS was exposing target 13 as part of a 3-d exposure (2016-02-16 23:25:25 until 2016-02-20 05:55:19). Coarse (64×64 , $1.25\ \mu\text{m}\ \text{pixel}^{-1}$) images of the centre of this target immediately showed that new particles had been collected. Since this time a number of scans have been performed to investigate the coverage of this target, in particular to constrain whether the collection represents a large number of individual dust particles or a multitude of fragments originating from a few larger particles impacting the target. These scans are ongoing and the values presented here may change as more data is analysed.

Data have been processed by performing a polynomial plane subtraction and median line correction to remove the scanner-sample slope and correct for distortions during the scan. Particles have then been manually identified and masked. Some areas have no corresponding pre-exposure scans; in these cases it cannot be excluded that the particles are contaminants. However, the morphology of dust on this target is so different from any contaminant detected to date, that the probability of contamination is low. None the less detections smaller than 3 pixels have been excluded here.

The area of the target scanned to date is $90\ 880\ \mu\text{m}^2$ and 135 particles have been identified with an areal coverage of 4.2 per cent. The particle count does not attempt to separate impact fragments from individual particles since the coverage is not yet sufficient to determine this, and thus represents an upper limit. For this reason, a true size distribution of the particles prior to collection cannot yet be established. Instead, some limits are given based on the effective diameters (the diameter of a circle having the same projected area as the particle) of the collected particles or fragments. Ninety per cent have an effective size less than $9.3\ \mu\text{m}$ and 50 per cent less than $3.7\ \mu\text{m}$.

2.10 Ground-based observations

Hundreds of ground-based observers, both professional and amateur, have an interest in observing 67P because their data complement the *in situ* observations by Rosetta. In the following paragraph we present data obtained from a 30 cm amateur telescope and a professional group with a 60 cm telescope. We also report results from a second professional group with a 2 m telescope.

The Rosetta amateur observer campaign (<http://rosetta.jpl.nasa.gov/rosetta-ground-based-campaign>) provides a link between amateur astronomers and the ESA/Rosetta mission. The image provided by Efrain Morales (Fig. 14) shows the coma and tail about 10 d after the outburst. Most of the dust particles seen in the image were emitted after the perihelion passage in summer 2015. However, big mm and cm sized particles from the 2009 perihelion passage also contribute to the brightness in the trail. Particles emitted during the outburst on 2016 Feb 19 populate the bright central portion of the image.

The robotic 0.6-m telescope TRAPPIST (TRANSiting Planets and Planetesimals Small Telescope; Jehin et al. 2011) is located at ESO’s La Silla Observatory. It is equipped with an FLI ProLine PL3041-BB camera with $2\text{k} \times 2\text{k}$ pixels of $15\ \mu\text{m}$. Used with the 2×2 binning mode it results in a pixel scale of $1.3\ \text{arcsec}$ and a field of view of 22 arcmin. The observations of comet 67P have been performed once or twice a week in 2016 with a Johnson–Cousins Rc filter and with exposure times ranging from 180 to 240 s. TRAPPIST images are reduced following a standard procedure described in Opitom et al. (2015). The sky background is subtracted and the photometric calibration is performed using

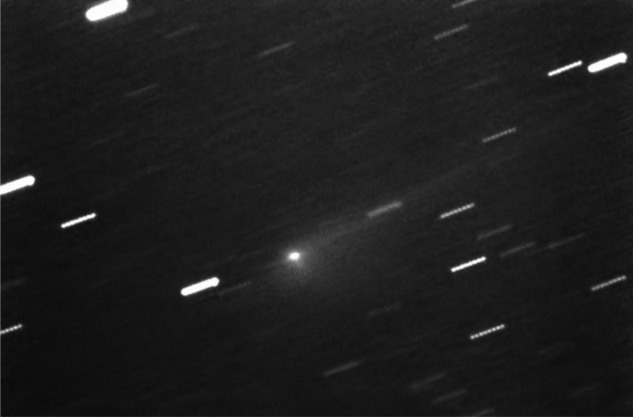


Figure 14. Image of 67P taken on 2016 Feb 29 05:39 UTC taken by Efrain Morales with the 30 cm LX200ACF telescope at Jaicoa Observatory, Puerto Rico, U.S.A.. The CCD image was obtained with a total exposure time of 54 min through a Baader IR filter. The scale of the image is 2.1×1.4 million km; the length of the star tracks corresponds to $\sim 120\,000$ km at the comet's distance.

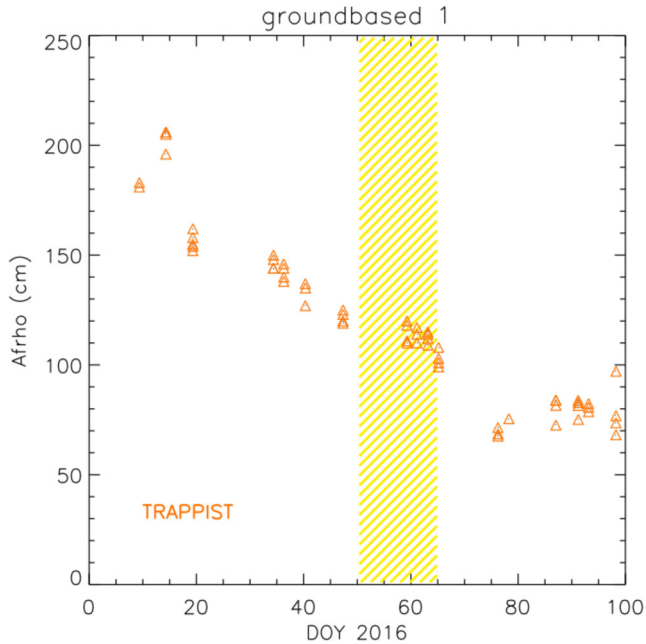


Figure 15. Corrected $Af\rho$ parameters of 67P for the time period from 2016 Jan 9 to April 7 obtained from observations with the TRAPPIST telescope for apertures of 5000 km. The yellow area marks the times when all burst particles with speeds ≥ 4 m s $^{-1}$ are within the aperture.

regular observations of photometric standard stars. The $Af\rho$ parameter (A'Hearn et al. 1984) is computed at a physical distance from the comet of 5000 km (Fig. 15). The observed brightness has been corrected for the varying phase angle (Sun-67P-observer) using a phase function that is the composite of two different empirical phase functions from Schleicher, Millis & Birch (1998) and Marcus (2007). During the first 100 d of 2016 the phase angle varied from 28° at the beginning of that period, through to a minimum phase angle of 4° at opposition, and finally to 9° at the end of that period. After 2016 Feb 19 the coma brightnesses in a 5000 km aperture show a clear increase of 25 per cent over values from earlier observations. This increased brightness was observed between February 29 and March 6. The beginning of the brightness increase cannot be

precisely determined because of bad weather in the days following the February 19 outburst. On March 17, the brightness values are back to the normal trend. However, not much of this brightness enhancement remains after the application of the phase correction because of the opposition surge of the applied empirical phase function, which was derived for observations of 1P/Halley (Schleicher et al. 1998). The phase correction at low phase angles is rather imperfect and may change after careful comparison with Rosetta observations (see below).

Boehnhardt et al. (2016) report 67P observations with the 2 m telescope on the Mt Wendelstein observatory of the University Observatory Munich. Their brightness values after 2016 Feb 19 deviate clearly beyond measurement uncertainty from the brightness trend using a fit to the earlier observations. However, application of a special phase function reduced the effect of the outburst. Contrary to an earlier outburst of 67P (2015 August 22-23), on 2016 Feb 21-22 the 67P coma appeared to be undisturbed in terms of geometric dust structures and radial gradient, except for an increase in the brightness.

In Fig. 15 the phase corrected $Af\rho$ data are compared with the time period (shown by yellow stripes) when all burst particles with speeds ≥ 4 m s $^{-1}$ are still within the aperture. The observations may show a ~ 10 per cent increase of $Af\rho$ (~ 10 cm) in the burst period compared with the values before the outburst. Later observations display the expected decrease of $Af\rho$ with heliocentric distance and time.

The long lasting ‘bump’ in the brightness of the comet as seen in the TRAPPIST and in other data sets (Boehnhardt et al. 2016; Snodgrass et al., in preparation) is coincident with the outburst, but also with the comet being at opposition. It may therefore be a combination of a geometric effect and the prolonged increase in activity. There is some indication that the departure from a smooth decrease in $Af\rho$ starts before February 19.

To estimate the total dust mass from the increased coma brightness observed with TRAPPIST, we assume that the increase in phase-corrected $Af\rho$ by approximately 10 cm observed around 2016 Feb 19 was due to dust released during the outburst on February 19. With $Af\rho = 4ps^2N/\rho$ (Müller 1999) and assuming a geometric albedo of $p = 0.05$, mean particle radius $s = 100$ μm , and aperture radius of $\rho = 5000$ km, we find $N = 2.5 \times 10^{11}$ particles in the aperture, corresponding to a total dust mass of 10^3 kg for a bulk density of 1000 kg m $^{-3}$.

3 DISCUSSIONS

In this section we describe the timing and duration of the outburst that was observed by the different instruments, and we discuss what this can tell us about the properties of the material released by this event. At first we start with the time relation of the data, secondly, we try to identify the time and source region of the outburst, and thirdly, we discuss the magnitude of the outburst. In order to do this we have to make some (not necessarily unanimously agreed) ad hoc assumptions just for the purpose to demonstrate the interrelations between the various observables. Eventually, such assumptions have to come from a comprehensive model of the outburst which is not the task of this first paper.

3.1 Time relation of the data

Timing and duration of the outburst can be investigated because the clocks for the different instruments are synchronised with the spacecraft clock. The flight control team makes sure that the spacecraft

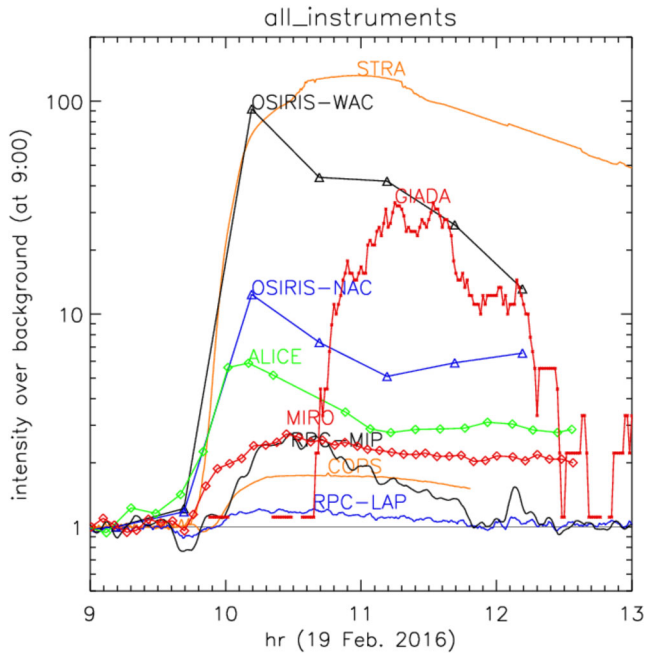


Figure 16. Intensity ratio of the measured parameters over the intensity measured at 9:00.

clock and ground time (UTC) is accurate within less than ~ 10 ms. The measurement of any parameter takes a certain amount of time, which is called the integration time. If the integration time is short (< 1 s), then this is of no concern here. Even if the measurement only takes a short time, the time tagging and the sampling of the available telemetry data points may be much less frequent than that. In the case of the data discussed here we assume that the accuracy of the sampling is of the order of a few seconds. Some images have longer integration times, which can be identified using the image data products, which carry a PDS label keyword `IMAGE_TIME` in the filename that refers to the middle of the integration time. The start and stop time of the integration are given by the `START_TIME` and `STOP_TIME` keywords in the image label files.

All measured parameters discussed above are displayed in Fig. 16 from 9:00 to 13:00 on 2016 Feb 19. For any given time the ratio of the intensity over the background value at 9:00 is displayed. Most parameters reached their maximum between 10:00 and 11:00. The intensity enhancements during the outburst ranged from ~ 20 per cent (RPC-LAP) to a factor of 130 (STR-A). The parameter values at 9:00 and at maximum are also given in Table 1.

The majority of the observations refer to the dust emitted in the outburst (Fig. 17). These dust observations display a significant

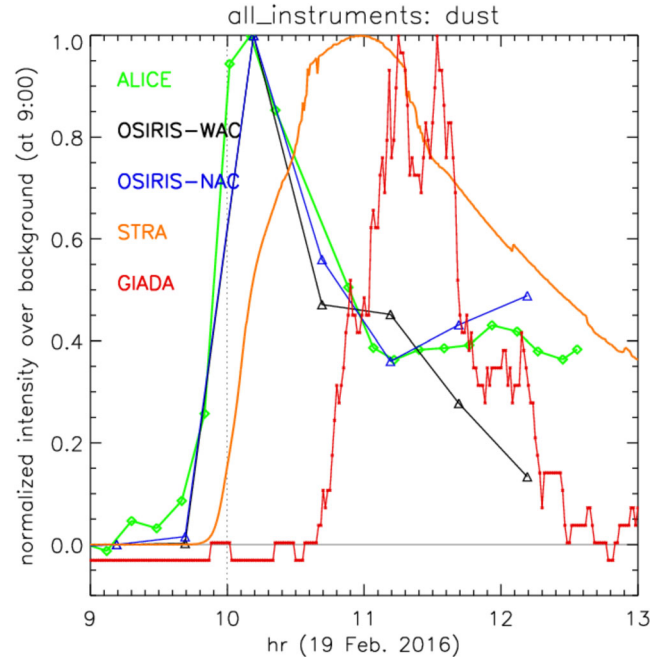


Figure 17. Normalized intensity (to maximum) of dust observations.

time lag between the observations by different instruments. The first signature was the dust cloud in the WAC images at 9:40. The next was the significantly enhanced coma brightness (≥ 10 per cent of max. value above background) observed by Alice at 9:51 followed at 9:58 by STR-A. Maximum brightness was observed by the OSIRIS WAC and NAC at 10:10. The GIADA smoothed count rate exceeded 10 per cent of maximum value above background at 10:42, and the trailed NAC images of near-by individual grains were observed at and after 11:40.

The enhanced coma brightnesses observed by Alice and OSIRIS refer to dust near the nucleus and their order is mostly determined by the respective sequence of observations. In contrast, the enhanced signatures in the STR-A, GIADA, and OSIRIS near-by grain data represent a clear time-of-flight relation of grains of different sizes and emission speeds. The mean speed of the GIADA grains (`GDS_IS`) is 6.5 m s^{-1} and the mean mass is $4 \times 10^{-8} \text{ kg}$, which corresponds to a radius of about $180 \text{ }\mu\text{m}$ (at an assumed density of 1000 kg m^{-3}).

For the STR-A camera to see any dust from the outburst, the emitted grains had to have traversed the distance of $\sim 30 \text{ km}$ from the nucleus to the STR-A FOV. Therefore, the fastest particles that were seen by STR-A had to have a speed of at least 25 m s^{-1} . The

Table 1. Measurement parameters at 9:00 and at maximum.

Instrument	Parameter	Value at 9:00	Maximum value	Factor	Time at maximum
OSIRIS WAC	Surface brightness [$\text{W m}^{-2} \text{ sr}^{-1} \text{ nm}^{-1}$]	5.1×10^{-7}	4.7×10^{-5}	91.9	10 : 11.5
OSIRIS NAC	Surface brightness [$\text{W m}^{-2} \text{ sr}^{-1} \text{ nm}^{-1}$]	1.75×10^{-6}	2.17×10^{-5}	12.3	10 : 11.5
Alice	Surface brightness [rayleighs]	84.0	494.1	5.88	10 : 10.1
MIRO	Antenna temperature in the H_2^{16}O line [K]	19.4	53.0	2.73	10 : 26.9
RPC LAP	Spacecraft potential [V]	-16.7	-20.3	1.22	10 : 38.6
RPC MIP	Electron density [cm^{-3}]	~ 440	~ 1200	2.7	10 : 37.6
ROSINA COPS	Gas density [cm^{-3}]	0.83×10^8	1.49×10^8	1.80	10 : 45.3
STR-A	Brightness [$\text{W m}^{-2} \text{ sr}^{-1} \text{ nm}^{-1}$]	2.6×10^{-8}	3.43×10^{-6}	132.1	10 : 58.2
GIADA	Dust count rate [min^{-1}]	0.1	3.33	33.3	11 : 15.0

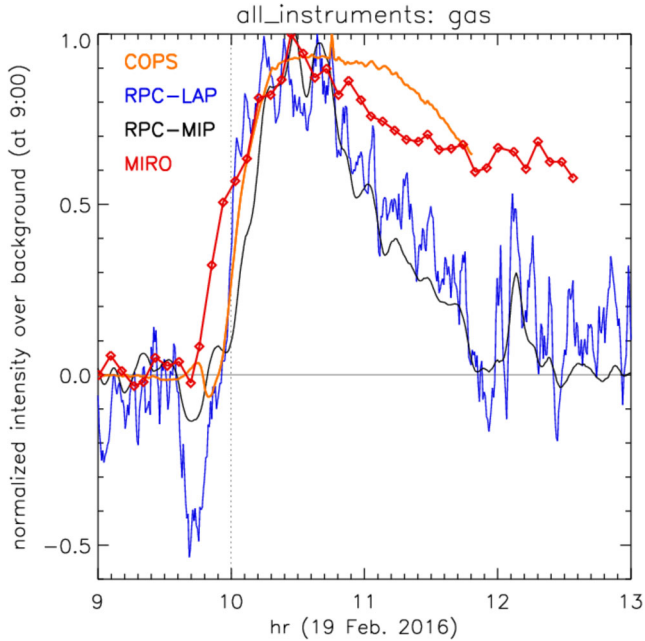


Figure 18. Normalized intensity (to maximum) of gas and plasma observations.

majority of them had speeds between 5 and 10 m s⁻¹. Similarly, the particles that had trails in the OSIRIS images had speeds of ≤ 4 m s⁻¹.

If we assume a speed-radius dependence of $v \sim s^{-0.5}$ then the particle sizes range from ~ 10 μm for the fastest STR-A particles to ~ 300 μm for the OSIRIS individual particles. The smallest particles (≤ 10 μm) were those collected by MIDAS.

The earliest indication of gas in the outburst was observed by MIRO at 9:52 (Fig. 18). This is within a minute of the earliest dust observations by Alice. Both LOSs are very close to each other. However, Alice measurements refer to dust near the nucleus while the MIRO signal is assumed to originate near Rosetta.

ROSINA COPS detected significant gas density increase (>10 per cent of maximum) at the position of Rosetta at 9:57. There was a small dip in the gas density (~ 10 per cent of the following enhancement) for ~ 10 min just prior to the strong rise of the signal.

RPC-MIP observed an increase of the electron density at Rosetta at 10:00. However, a significant reduction of the electron density started already at 9:38, just at the expected time of the outburst. The dip in the electron density had an amplitude of ~ 15 per cent of the following enhancement.

The spacecraft potential monitored by RPC-LAP followed closely the course of the electron density becoming more negative at higher electron densities. At 9:00 the mean S/C potential was about -16.7 V; by 9:42 it was -15 V and became rapidly more negative reaching -20 V around 10:20. During the following 3 h the S/C potential excursion decreased to the normal value of ~ -16 V.

3.2 Time and source region of the outburst

The first sign of the outburst was seen at 9:40 in the OSIRIS image (Fig. 3) close to the shadow region. Fig. 19 shows the same image with isophotes. The bottom centre brightness originates from the dust cloud that was generated in the outburst and became illuminated

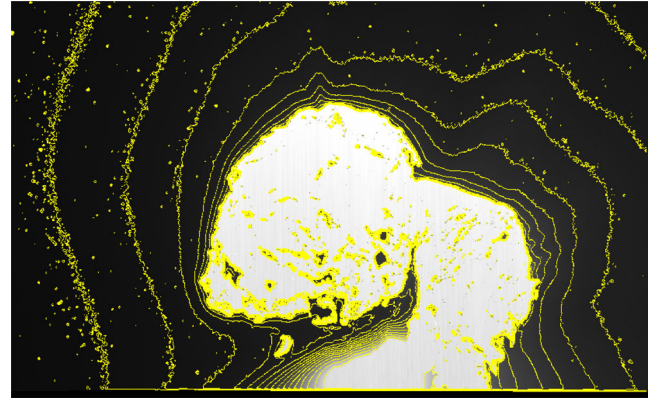


Figure 19. OSIRIS WAC image at 9:40 with isophotes. The isophotes are separated by a factor 1.4 with the innermost isophote at a brightness of 10.54×10^{-5} W m⁻² sr⁻¹ nm⁻¹ (just below the saturation limit).

by the Sun. Fig. 2 shows the model scene with the complete nucleus and the shadow at 9:40 but without the dust cloud.

The potential source region is in the centre at or below the edge of the WAC image (in region Seth, Anubis, or Atum). The brightness of the dust cloud is in saturation. Most of the scene below the WAC image is in the shadow except for a cliff that just appeared in full sunlight. The gradient of the isophotes in the lower part of the image (Fig. 19) points to a maximum brightness close to the illuminated cliff which is ~ 700 m below the edge of the image. At an expansion speed of ~ 25 m s⁻¹ the time for the cloud to enter the FOV of the WAC camera is $\lesssim 120$ s. This brings the outburst time to 9:38 ± 1 min. The centre coordinates of the illuminated cliff are in the Atum region at longitude 232°3, latitude $-28^{\circ}6$, and radius 1738 m.

The outburst started close to the morning terminator and the source region rotated at a rate of $\sim 30^{\circ}$ h⁻¹ into the Sun direction; at about 13:00 on Feb 19 the source region was near the sub-solar limb and at about 16:00 the source region reached the evening terminator and entered comet night.

3.3 Magnitude of the outburst

The peak brightnesses observed by Alice and OSIRIS provide a means to estimate the magnitude of the outburst. The increase in mean coma brightness in the 175–195 nm bandpass is ~ 370 rayleighs. This translates to a radiance of $I = 1.58 \times 10^{-8}$ W m⁻² nm⁻¹ sr⁻¹ at 185.5 nm. The solar radiance at 185.5 nm and at 2.4 au is 1.58×10^{-4} W m⁻² nm⁻¹ sr⁻¹ so $I/F = 1.0 \times 10^{-4}$. From OSIRIS NAC we find $I/F \sim 3 \times 10^{-5}$ before the outburst and $\sim 2 \times 10^{-4}$ after the outburst, in good agreement with the Alice result. The filling factor, or optical depth, τ , is given by $I/F = pj(\alpha)\tau$, where p is the geometric albedo and $j(\alpha)$ is the phase function. Assuming that the dust has the same properties as the nucleus (Feaga et al. 2015), $p = 0.04$, $j(63^{\circ}) = 0.10$, so $\tau = 0.025$. OSIRIS WAC finds $\tau = 0.01$ before and $\tau = 0.1$ immediately after the outburst. This difference is not surprising since the LOSs of both instruments are different in relation to the centre of the outburst. Future detailed analysis and modelling the scattering properties of dust of different sizes at different wavelengths along similar LOSs may provide information on the size distribution of the particles. In addition the total cross-section of particles generated in the outburst may be estimated by modelling the particles' emission.

There is another way to calculate the total cross-section of the emitted particles; this is from the *in situ* measurements by GIADA

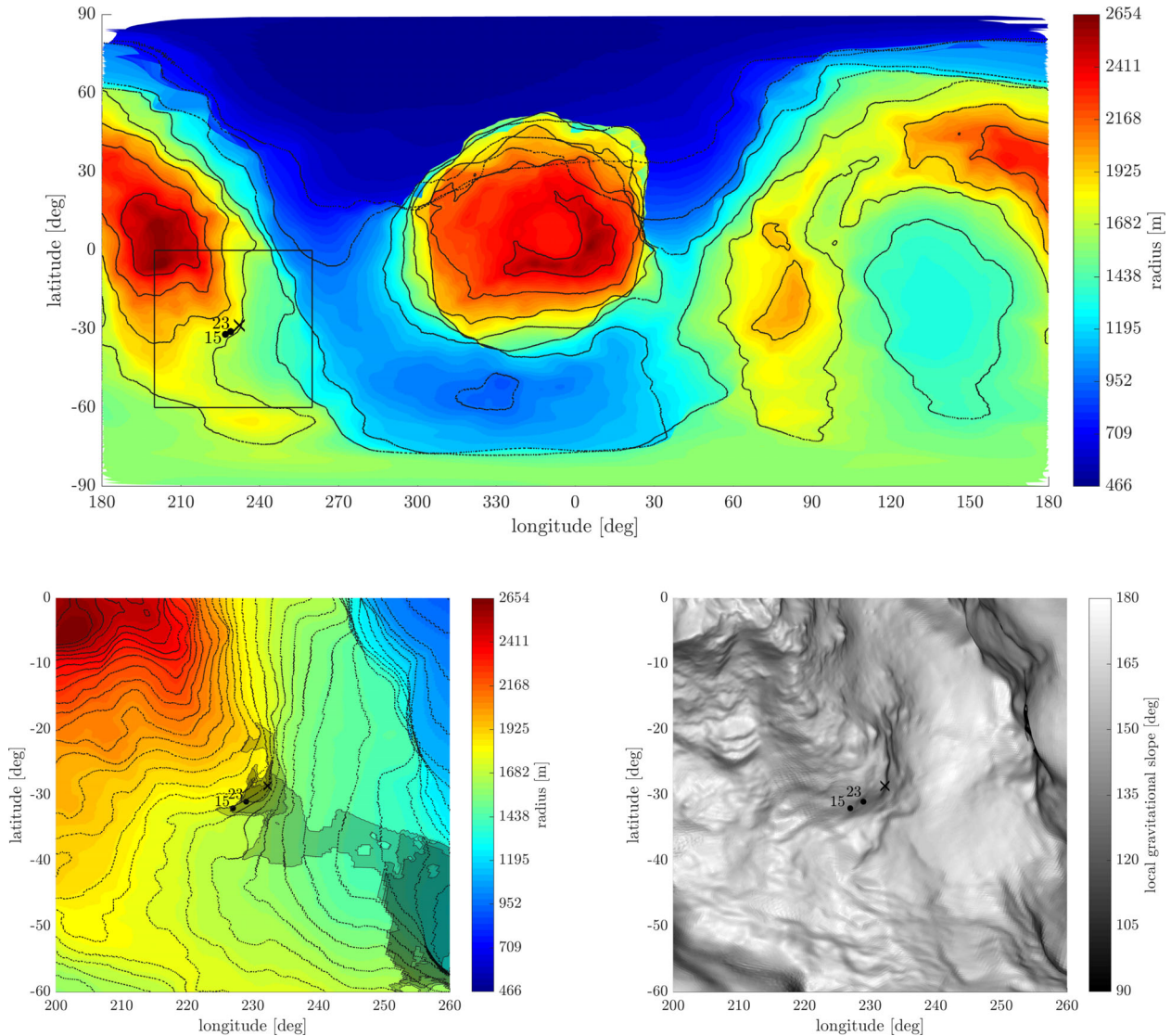


Figure 20. Terrain maps of 67P. Outburst positions are marked by X (2016 Feb 19 outburst) and by numbers (cf. Vincent et al. 2016b). Top: radius map showing the elevated head region in the centre and the body at the left (West) and right (East) fringes. Lower left: enlarged radius map showing the outburst position (x). The contour lines are separated by 50 m. Grey shading represent illuminated areas at 09:40 (dark grey), 09:50 (middle grey), and 10:00 (light grey). Lower right: topographic map in which the grey shading represents the local slope, accounting for gravity and centrifugal force (white=flat, black=vertical wall).

and MIDAS. MIDAS found an areal coverage of 4.2 per cent of bigger than $1 \mu\text{m}$ -radius particles. The total area of the GIADA IS detector is 10^{-2} m^2 . The total cross-section of all particles detected during the outburst by GIADA is $7 \times 10^{-6} \text{ m}^2$ corresponding to 1.2×10^{-3} coverage of $>100 \mu\text{m}$ -radius particles. Scaling the dust coverage to 2 km i.e. $\sim 1/20$ th of the Rosetta distance then an optical depth of 1 is reached. This value is compatible with the saturated brightness of the inner dust cloud in the OSIRIS WAC image at 9:40. If detailed analysis confirms these values then during the outburst the dominant cross-section is in the MIDAS particles of radius $<100 \mu\text{m}$.

The total mass of $>100 \mu\text{m}$ -radius particles detected by the 10^{-2} m^2 GIADA IS and GDS sensors at 35 km from the nucleus is $1.33 \times 10^{-6} \text{ kg}$. If we assume that a similar mass flux of dust particles was emitted into a solid angle $\Omega_d = 1 \text{ sr}$ then the total mass is $M_{100 \mu\text{m}} = 1.6 \times 10^3 \text{ kg}$ not counting any mass contribution by smaller and much bigger particles. This mass is about 1.6 times the

mass derived from $Af\rho$ measurements in ground-based observations (Section 2.10). The width of the emission was therefore probably narrower than assumed above. The interpretation of the ground-based observations may also be improved by the comparison with Rosetta observations.

Similarly, the gas production can be estimated from the measured extra gas density $n_g \sim 5 \times 10^7 \text{ cm}^{-3}$ at Rosetta. We assume that the gas from the outburst is emitted into a solid angle $\Omega_g = 2\pi \text{ sr}$ with a speed $v_g \sim 600 \text{ m s}^{-1}$. The gas production rate in the outburst is then $Q_g = \Omega_g r_{\text{ROS}}^2 v_g n_g \approx 2.3 \times 10^{26} \text{ s}^{-1}$ corresponding to $\sim 10 \text{ kg s}^{-1}$ H_2O , CO_2 , and CO . The duration of the enhanced gas density was about 2 h; therefore a total of $\sim 7 \times 10^4 \text{ kg}$ of gas was emitted during the outburst. This exceeds the total amount of dust detected by GIADA by at least a factor of 40, giving a lower limit for the dust-to-gas-mass-ratio of ~ 0.025 . During the background emission Fulle et al. (2016) estimate the dust-to-gas-mass-ratio to be ~ 6 or larger.

4 CONCLUSIONS

The outburst on 2016 Feb 19 was unexpected, but serendipitously most Rosetta instruments were in suitable measuring conditions while the outburst unfolded. This was very special because for the many outbursts during perihelion passage (2015 July to September, Vincent et al. 2016b) we never had the situation that that many instruments observed the same outburst at once. In particular, the *in situ* dust instruments did not make significant observations of these outbursts. This was due to the large distances (up to 400 km) Rosetta had to maintain for safety reasons. The unique circumstances of the February 19 outburst enabled the *in situ* instruments to provide important measurements to quantify the outburst.

The likely outburst location in the Atum region at latitude -28.6° and longitude $+232.3^\circ$ (Fig. 20) is interesting because two other outbursts observed in 2015 were in the immediate vicinity (Vincent et al. 2016a). They were outburst no. 15 observed by NAVCAM on 2015-08-01T15:44 at latitude $= -32^\circ$, longitude $= +227^\circ$ and no. 23 observed by OSIRIS-NAC on 2015-08-28T13:36 at latitude $= -31^\circ$, longitude $= +229^\circ$.

The location of these outbursts is on the eastern slope of the body of 67P. It is in a region of a steep cliff to the east. The fact that the outburst started when this region just exited the shadow from the head suggests that thermal stress in the surface material may have triggered a landslide that exposed fresh (water) ice to direct solar illumination. Also other features of the observations support that idea: (1) the relative long duration of the GIADA dust impact phase which tells that the dust cone is very broad, (2) from looking at OSIRIS pictures, where one sees a cloud, not a narrow jet (3) from the fact that it is probably driven by water only. In this scenario the trigger of activity is thermal stress together with fracture mechanics and gravity in form of landslides or avalanches before solar heat can release gas from fresh ice which in turn accelerates dust released during this process.

At present, it is difficult to infer the nature of the icy material exposed to solar illumination. Recent simulations show that, in addition to sublimation of crystalline ice, clathrate destabilization and amorphous ice crystallization can lead to the formation of outbursts and pits with shapes consistent with those observed in the Seth region (Mousis et al. 2015). A proof of these ideas would come from the composition of the gas during this outburst. If the gas is lacking highly volatile species such as CO, N₂ or Ar, it would mean that the sublimating icy layer is close to the surface and was already partly devolatilized before, as shown by thermal evolution models (Mousis et al. 2015). Part of it could even be reprocessed water ice. In this case the outburst was not the ‘jet’ revealing fresh material from the interior, but just a surface effect. It may look completely different from the gas composition perspective than the outbursts last summer, where all volatiles except water peaked.

A further interesting feature of this outburst is that the gas production decreased much faster than expected from direct solar illumination. This may suggest that building up of a dust mantle quenched the gas emission. This outburst will trigger many further studies in the near future.

ACKNOWLEDGEMENTS

Rosetta is an ESA mission with contributions from its member states and NASA. Rosetta’s Philae lander is provided by a consortium led by DLR, MPS, CNES and ASI. We thank all elements of the Rosetta project for the magnificent job they are doing to make this mission an astounding success. The Alice team

acknowledges continuing support from NASA’s Jet Propulsion Laboratory through contract 1336850. GIADA/Univ Parthenope NA/INAF/OAC/IAA/INAF-IAPS: this research was supported by the Italian Space Agency (ASI) within the ASI-INAF agreements I/032/05/0 and I/024/12/0. OSIRIS was built by a consortium of the Max-Planck- Institut für Sonnensystemforschung, Göttingen, Germany, CISAS University of Padova, Italy, the Laboratoire d’Astrophysique de Marseille, France, the Instituto de Astrofísica de Andalucía, CSIC, Granada, Spain, the Research and Scientific Support Department of the European Space Agency, Noordwijk, The Netherlands, the Instituto Nacional de Técnica Aeroespacial, Madrid, Spain, the Universidad Politécnica de Madrid, Spain, the Department of Physics and Astronomy of Uppsala University, Sweden, the UK(STFC), and the Institut für Datentechnik und Kommunikationsnetze der Technischen Universität Braunschweig, Germany. The support of the national funding agencies of Germany (DLR), France(CNES), Italy(ASI), Spain(MEC), Sweden(SNSB), and the ESA Technical Directorate is gratefully acknowledged. Work at LPC2E/CNRS was supported by CNES and by ANR under the financial agreement ANR-15-CE31-0009-01. Work on ROSINA COPS at the University of Bern was funded by the State of Bern, the Swiss National Science Foundation and by the European Space Agency PRODEX program. OM: this work has been partly carried out thanks to the support of the A*MIDEX project (n° ANR-11-IDEX-0001-02) funded by the ‘Investissements d’Avenir’ French Government program, managed by the French National Research Agency (ANR). This work also benefited from the support of CNRS-INSU national program for planetology (PNP).

REFERENCES

- A’Hearn M. F., Schleicher D. G., Millis R. L., Feldman P. D., Thompson D. T., 1984, *AJ*, 89, 579
 Balsiger H. et al., 2007, *Space Sci. Rev.*, 128, 745
 Bentley M. S. et al., 2016, *Nature*, 537, 73
 Bieler A. et al., 2015, *A&A*, 583, A7
 Boehnhardt H. et al., 2016, *MNRAS*, in press
 Buemi M., Landi A., Procopio D., 2000, *ESA Spec. Publ.*, 425, 279
 Burch J. L., Goldstein R., Cravens T. E., Gibson W. C., Lundin R. N., Pollock C. J., Winningham J. D., Young D. T., 2007, *Space Sci. Rev.*, 128, 697
 Carr C. et al., 2007, *Space Sci. Rev.*, 128, 629
 Colangeli L. et al., 2007, *Space Sci. Rev.*, 128, 803
 Della Corte V. et al., 2014, *J. Astron. Instrum.*, 03, 1350011
 Della Corte V. et al., 2015, *A&A*, 583, A13
 Della Corte V. et al., 2016a, *Acta Astron.*, 126, 205
 Della Corte V. et al., 2016b, *MNRAS*, in press
 Eriksson A. I. et al., 2007, *Space Sci. Rev.*, 128, 729
 Feaga L. M. et al., 2015, *A&A*, 583, A27
 Feldman P. D. et al., 2015, *A&A*, 583, A8
 Ferrari M., Della Corte V., Rotundi A., Rietmeijer F. J. M., 2014, *Planet. Space Sci.*, 101, 53
 Fulle M. et al., 2015, *ApJ*, 802, L12
 Fulle M., Altobelli N., Buratti B., Choukroun M., Fulchignoni M., Grün E., Taylor M. G. G. T., Weissman P., 2016, *MNRAS*, 462, S2
 Geiger B., Barthelmy, 2016, ROSETTA ORBITER NAVCAM EXT1-MTP026, RO-C-NAVCAM-2-EXT1-MTP026-V1.0, ESA Planetary Science Archive and NASA Planetary Data System
 Glassmeier K.-H., Boehnhardt H., Koschny D., Kürt E., Richter I., 2007a, *Space Sci. Rev.*, 128, 1
 Glassmeier K.-H. et al., 2007b, *Space Sci. Rev.*, 128, 649
 Gulkis S. et al., 2007, *Space Sci. Rev.*, 128, 561
 Hässig M. et al., 2015, *Science*, 347, aaa0276
 Jehin E. et al., 2011, *The Messenger*, 145, 2
 Keller H. U. et al., 2007, *Space Sci. Rev.*, 128, 433
 Marcus J. N., 2007, *International Comet Quarterly*, 29, 39

- Mousis O. et al., 2015, *ApJ*, 814, L5
 Müller M., 1998, *ESOC Report RO-ESC-TA-5501*.
 Opatom C., Jehin E., Manfroid J., Hutsemékers D., Gillon M., Magain P., 2015, *A&A*, 584, A121
 Riedler W. et al., 2007, *Space Sci. Rev.*, 128, 869
 Rotundi A. et al., 2015, *Science*, 347, aaa3905
 Schleicher D. G., Millis R. L., Birch P. V., 1998, *Icarus*, 132, 397
 Sierks H. et al., 2015, *Science*, 347, aaa1044
 Stern S. A. et al., 2007, *Space Sci. Rev.*, 128, 507
 Stern S. A. et al., 2015, *Icarus*, 256, 117
 Trotignon J. G. et al., 2007, *Space Sci. Rev.*, 128, 713
 Vincent J.-B. et al., 2016a, *A&A*, 587, A14
 Vincent J.-B. et al., 2016b, *MNRAS*, 462, S184
- ¹Max-Planck Institut für Kernphysik, Saupfercheckweg 1, 69127 D-Heidelberg, Germany
²Laboratory for Atmospheric and Space Physics, University of Colorado, 1234 Innovation Dr, Boulder, CO 80303, USA
³Max-Planck Institut für Sonnensystemforschung, Justus-von-Liebig-Weg, 3 D-37077 Goettingen, Germany
⁴European Space Agency (ESA), Camino Bajo del Castillo, s/n, E-28692 Villanueva de la Canada, Madrid, Spain
⁵Physikalisches Institut, University of Bern, Sidlerstr. 5, CH-3012 Bern, Switzerland
⁶Space Research Institute, Austrian Academy of Sciences, Schmiedlstraße 6, A-8042 Graz, Austria
⁷LESIA-Observatoire de Paris, CNRS, UPMC, Université Paris-Diderot, 5 place Jules Janssen, F-92195 Meudon, France
⁸IAPS/INAF, Via del Fosso del Cavaliere, Roma I-00133, Italy
⁹Swedish Institute of Space Physics, Ångström Laboratory, Lägerhyddsvägen 1, Uppsala, Sweden
¹⁰Department of Physics and Astronomy, Johns Hopkins University, Baltimore, MD, USA
¹¹Imperial College, South Kensington Campus, London SW7 2AZ, UK
¹²Institute for Geophysics and Extraterrestrial Physics, TU Braunschweig, D-38106 Braunschweig, Germany
¹³LPC2E, CNRS, Orléans, France
¹⁴Jet Propulsion Laboratory/Caltech, 4800 Oak Grove Drive, Pasadena, CA 91109, USA
¹⁵Institut d'Astrophysique et de Géophysique, Université de Liège, Sart-Tilman, B-4000 Liège, Belgium
¹⁶Jaicoa Observatory, Aguadilla, Puerto Rico, USA
¹⁷LAM (Laboratoire d'Astrophysique de Marseille) UMR 7326, Aix Marseille Université, CNRS, F-13388 Marseille, France
¹⁸ESA/ESOC, Robert-Bosch-Str. 5, Darmstadt, Germany
¹⁹Dip. di Scienze e Tecnologia, Università degli Studi di Napoli Parthenope, CDN IC4, I-80143 Naples, Italy
²⁰Institute of Physics, University of Graz, Universitätsplatz 3, A-8010 Graz, Austria
²¹Institut für Raumfahrtssysteme (IRS), Universität Stuttgart, Pfaffenwaldring 29, D-70569 Stuttgart, Germany
²²Planetary and Space Sciences, Department of Physical Sciences, The Open University, Milton Keynes MK7 6AA, UK
²³Space Science Institute, 13456 Cajon Creek Court, Rancho Cucamonga, CA 91739, USA
²⁴Department for Astronomy, University of Maryland, College Park, MD 20742-2421, USA
²⁵Department of Physics and Astronomy 'G. Galilei', University of Padova, Vic. Osservatorio 3, I-35122 Padova, Italy
²⁶LATMOS, CNRS/UVSQ/IPSL, 11 Boulevard d'Alembert, F-78280 Guyancourt, France
²⁷Centro di Ateneo di Studi ed Attività Spaziali 'Giuseppe Colombo' (CISAS), University of Padova, Via Venezia 15, I-35131 Padova, Italy
²⁸Southwest Research Institute, 6220 Culebra Rd., San Antonio, TX 78238, USA
²⁹European Space Research and Technology Centre, European Space Agency, Keplerlaan 1, NL-2201 AZ Noordwijk, the Netherlands
³⁰INAF Osservatorio Astronomico di Padova, Vicolo dell'Osservatorio 5, I-35122 Padova, Italy
³¹CNR-IFN UOS Padova LUXOR, Via Trasea 7, I-35131 Padova, Italy
³²Department of Physics and Astronomy, Uppsala University, Box 516, SE-75122 Uppsala, Sweden
³³Department of Industrial Engineering University of Padova Via Venezia, 1, I-35131 Padova, Italy
³⁴INAF-Osservatorio Astronomico, Via Tiepolo 11, I-34143 Trieste, Italy
³⁵Instituto de Astrofísica de Andalucía-CSIC, Glorieta de la Astronomía, E-18008 Granada, Spain
³⁶Institute of Planetary Research, DLR, Rutherfordstrasse 2, D-12489 Berlin, Germany
³⁷Institute for Space Science, National Central University, 32054 Chung-Li, Taiwan
³⁸Laboratoire d'Astrophysique de Marseille, UMR 7326 CNRS and Aix-Marseille Université, 38 rue Frédéric Joliot-Curie, F-13388 Marseille cedex 13, France
³⁹Instituto de Astrofísica de Andalucía (CSIC), Glorieta de la Astronomía s/n, E-18008 Granada, Spain
⁴⁰INAF-OAR, Via Frascati 33, Monte Porzio Catone, Roma I-00078, Italy
⁴¹Department of Information Engineering, University of Padova, Via Gradenigo 6/B, I-35131 Padova, Italy
⁴²Southwest Research Institute, 1050 Walnut Street, Suite 300, Boulder, CO 80302, USA
⁴³PAS Space Research Center, Bartycka 18A, PL-00716 Warszawa, Poland
⁴⁴International Space Science Institute, Hallerstrasse 6, CH-3012 Bern, Switzerland
⁴⁵Johns Hopkins University Applied Physics Laboratory, Laurel, MD, USA
⁴⁶Planetary Science Institute, 1700 East Fort Lowell, Suite 106, Tucson, AZ 85719, USA
⁴⁷Laboratoire de Météorologie Dynamique, 4 place Jussieu, Sorbonne Universités, UPMC Univ Paris 06, CNRS, F-75252 Paris, France

This paper has been typeset from a $\text{\TeX}/\text{\LaTeX}$ file prepared by the author.